Bioactive Materials 21 (2023) 86–96

Contents lists available at ScienceDirect

Bioactive Materials

journal homepage: www.keaipublishing.com/en/journals/bioactive-materials

In situ forming oxygen/ROS-responsive niche-like hydrogel enabling gelation-triggered chemotherapy and inhibition of metastasis

Shi-Xiong Chen [a,b,1], Ji Zhang [d,e,f,g,1], Fengfeng Xue [a], Wei Liu [d,e,f,g], Yichen Kuang [a,b], Bingxin Gu [d,e,f,g], Shaoli Song [d,e,f,g,**], Hangrong Chen [a,b,c,*]

[a] State Key Laboratory of High Performance Ceramics and Superfine Microstructures, Shanghai Institute of Ceramics, Chinese Academy of Sciences, Shanghai, 200050, PR China
[b] Center of Materials Science and Optoelectronics Engineering, University of Chinese Academy of Sciences, Beijing, 100049, PR China
[c] School of Chemistry and Materials Science, Hangzhou Institute for Advanced Study, University of Chinese Academy of Sciences, Sub-lane Xiangshan Road 1, Hangzhou, 310024, PR China
[d] Department of Nuclear Medicine, Fudan University Shanghai Cancer Center, Shanghai, 200032, PR China
[e] Department of Oncology, Shanghai Medical College, Fudan University, Shanghai, 200032, PR China
[f] Center for Biomedical Imaging, Fudan University, Shanghai, 200032, PR China
[g] Shanghai Engineering Research Center of Molecular Imaging Probes, Shanghai, 200032, PR China

ARTICLE INFO

Keywords:
Hypoxia-activated prodrugs
Bio-niches
Hypoxia-inducible hydrogels
Antimetastases

ABSTRACT

Though the development of the diverse hypoxia-activated prodrugs (HAPs) has made great progresses in the last several decades, current cancer therapy based on HAPs still suffers many obstacles, e.g., poor therapeutic outcome owing to hard deep reaching to hypoxic region, and the occurrence of metastasis due to hypoxia. Inspired by engineered niches, a novel functional chitosan polymer (CS-FTP) is synthesized for construction of a hydrogel-based bio-niche (CS-FTP-gel) in aiming at remodeling tumor hypoxic microenvironment. The CS-FTP polymers are crosslinked to form a niche-like hydrogel via enzyme-mediated oxygen-consumable dimerization after injected into tumor, in which a HAP (i.e., AQ4N) could be physically encapsulated, resulting in enhanced tumor hypoxia to facilitate AQ4N-AQ4 toxic transformation for maximizing efficacy of chemotherapy. Furthermore, Pazopanib (PAZ) conjugated onto the CS backbone via ROS-sensitive linker undergoes a stimuli-responsive release behavior to promote antiangiogenesis for tumor starvation, eventually contributing to the inhibition of lung metastasis and synergistic action with AQ4N-based chemotherapy for an orthotopic 4T1 breast tumor model. This study provides a promising strategy for hypoxia-based chemotherapy and demonstrates an encouraging clinical potential for multifunctional hydrogel applicable for antitumor treatment.

1. Introduction

Tissue hypoxia is a characteristic feature of solid tumors [1,2]. Owing to a relative imbalance and unorganized secretion of angiogenesis-associated factors in rapidly growing tumors, the consequent tumor vasculature is highly abnormal and results in an inadequate blood supply, eventually generating distinctive hypoxic regions in tumor where oxygen and nutrients are scarce [3,4]. As a hallmark of primary malignancies, hypoxia is strongly associated with propagation, malignant progression, and resistance to chemo/radio-therapy [5,6]. Notably, it is also a negative prognostic and predictive factor for patients with poor disease-free survival and local control [7], and it has thus become a central role in tumor physiology and cancer treatment. However, the very existence of hypoxia also provides a clue for tumor-selective diagnosis and therapy [8,9]. Many factors of the hypoxia-relevant pathway have been considered as good candidates for theranostic targets, such as reductase and hypoxia-inducible transcription factor 1 (HIF-1) [10,11]. Thus, several theranostic methods are now

Peer review under responsibility of KeAi Communications Co., Ltd.
* Corresponding author. State Key Laboratory of High Performance Ceramics and Superfine Microstructures, Shanghai Institute of Ceramics, Chinese Academy of Sciences, Shanghai, 200050, PR China..
** Corresponding author. Department of Nuclear Medicine, Fudan University Shanghai Cancer Center, Shanghai, 200032, PR China.
E-mail addresses: shaoli-song@163.com (S. Song), hrchen@mail.sic.ac.cn (H. Chen).
[1] These authors contributed equally to this work.

https://doi.org/10.1016/j.bioactmat.2022.08.002
Received 7 March 2022; Received in revised form 19 July 2022; Accepted 1 August 2022

vigorously being developed, including hypoxia-specific imaging, bioreductive prodrugs, hypoxia-regulated gene therapy, and HIF-1-targeted cancer therapy [12–14].

Among all methods, bioreductive prodrugs have been extensively explored as one of the most promising hypoxia-responsive anticancer therapy, thanks to its tumor-specific toxicity and direct killing effect [15,16]. Even in local administration, conventional chemotherapy drugs will extravasate out of the tumor tissue through the interstitial fluid and enter into systemic circulation, consequently damaging the normal tissue. Therefore, bioreductive prodrugs have advantage of selectivity both in systemic injection and local administration [17,18]. Thereinto, bioreductive prodrugs, also known as hypoxia-activated prodrugs (HAPs), are non-toxic in normoxic region and can be selectively activated to be toxic drugs in a hypoxia-dependent manner. In essence, nontoxicity-to-toxicity transition requires reductase-enabled one-electron reduction of a prodrug to a radical, which undergoes further reduction to an active drug that mediates cellular toxicity under hypoxia [19]. For example, AQ4N, the di-N-oxide of 1,4-bis[{2-(dimethylaminoethyl}-amino]5,8-dihydroxyanthracene-9,10-dione(AQ4), is a prodrug designed to be excluded from cell nuclei until bioreduced in hypoxic cells to AQ4, a DNA intercalator and topoisomerase II poison [20]. Thus, AQ4N is a highly selective drug that can be activated and is preferentially toxic to hypoxic cells in tumor. Although many clinical trials have been performed or are ongoing either as monotherapies or as part of combination therapies (e.g., AQ4N in Phase 1 clinical trial and TH302 in Phase 3 trial) [21,22], the development of HAPs is experiencing bottleneck in practice [23]. One major hindrance is the inability to reach hypoxic regions that are distant from blood vessel network, which results in inadequate exposure to antitumor HAPs and contributes to low efficient chemotherapy [24,25]. To overcome this native obstacle, strategies aimed at extending hypoxia area/elevating hypoxia level have been adopted using photosensitizers, vascular disrupting agents, and oxygen-depleting carriers [26–28]. However, aggravated hypoxia also can stimulate tumor metabolic reprogramming to promote cancer metastasis, which is another hindrance for hypoxia-based cancer therapy [29]. Therefore, novel hypoxia-reinforcement approaches, simultaneously providing antimetastasis potency are highly needed to further optimize HAPs-based therapeutic regimen. However, researches on hypoxia-regulatable prodrug delivery system meanwhile, particularly those possessing an ability to inhibit metastasis, have rarely been reported.

In the past decade, the nanoengineered immune niches that can reprogram the tumor microenvironment (TME) for cancer immunotherapy have been drawn into the limelight [30]. To some extent, nanoengineered immune niches is the nanotechnology-based synthetic delivery or depot platforms of immunomodulatory drugs, and is designed to change the immunesuppressive TME into immune-supportive milieu, leading to remarkably improved immunotherapeutic efficacy [31–33]. In particular, engineered niches consisting of synthetic hydrogels to reconstruct critical aspects of the natural extracellular matrix (ECM) have been considered as emerging paradigm in the mimicry of three-dimensional (3D) microenvironments and native extracellular niche [34,35]. Researchers have endeavored to exploit synthetic hydrogels-based niches with variable physico-chemical parameters, including cytokines and mechanical properties, to regulate cell behavior [36,37]. Hence, synthetic niches as a highly customizable platform might well serve as a 3D hypoxic microenvironment for HAPs-based chemotherapy.

In this work, inspired by engineered niches, a novel functional chitosan polymer (CS-FTP) was developed for constructing an injectable stimuli-responsive hydrogel-based niche-mimic (CS-FTP-gel). After ferulic acid (FA, namely F) and thioketal (TK, namely T) were conjugated onto chitosan (CS) backbone, we have successfully synthesized a new class of oxygen/reactive oxygen species (ROS)-responsive polymer (CS-FT) that can further covalently bind with antiangiogenic Pazopanib (PAZ, namely P) [38] using TK-containing moiety. The FA molecules conjugated onto the obtained CS-FTP can react with oxygen via enzyme-mediated chemical reaction [39] and then followed by dimerization of FA to achieve oxygen-triggered gelation. When administered intratumorally, the mixed solution of CS-FTP and a HAPs, AQ4N [40], will be injected together with enzyme (Laccase) to *in situ* form the hydrogel (CS-FTP-gel@AQ4N), enabling physically encapsulation of AQ4N and continuously consuming oxygen to induce hypoxia. Due to its excellent oxygen-scavenging capability, as illuminated in Fig. 1a, CS-FTP-gel @AQ4N could significantly enhance hypoxic microenvironment in tumor and thus result in increased toxic transformation of AQ4N to AQ4 for selective chemotherapy. Moreover, the TK bond of CS-FTP could be broken when exposed to ROS overexpressed in tumor region to execute sustained release of PAZ [41]. Regarding its phosphorylation-inhibitory action, PAZ could be acted as an inhibitor of the kinases VEGFR-1, -2 and -3, PDGFR-α, and -β, etc. [42] With binding to VEGFR/PDGFR family receptors that work in the induction of angiogenesis, PAZ can inhibit the tumor angiogenesis and further achieve tumor starvation and antimetastasis. The oxygen-depleting performance of the niche-mimic and the therapeutic efficacy of hypoxia-base chemotherapy, as well as the effect of CS-FTP-gel on inhibition of tumor pulmonary metastasis were detailedly evaluated. Such a novel platform to optimize HAPs-based chemotherapy through realizing hypoxia–inducible gelation and simultaneously mitigating tumor metastasis provides a new avenue in nanomedicine for precise and anti-metastatic tumor therapy, exhibiting promising prospects in clinical transformation.

2. Results and discussion

2.1. Design of CS-FTP

The CS-FTP polymers used in this study were synthesized with a chemical structure as schematically shown in Fig. 1b and c. According to literature report [39], we coupled carboxyl groups of FA to amine groups of CS via carbodiimide-mediated reaction. Then we prepared TK to serve as a ROS-responsive linker for second functionalization of CS and PAZ could further conjugate to carboxyl groups of TK to obtain the CS-FTP. ^{1}H nuclear magnetic resonance (NMR) measurement was performed to confirm the successful synthesis of TK and the structure of CS-FTP (Fig. S1). In details, the peak at ~1.52 ppm is corresponding to the –CH_3 and peaks around ~2.7 ppm are corresponding to the –CH_2 in the TK-containing linker. Other peaks are also observed including ~6.4 ppm, ~6.8 ppm, ~7.1 ppm and ~7.4 ppm corresponding to the –CH in FA segment. Moreover, the peaks at ~3.31 ppm, ~3.63 ppm, ~7.6 ppm and ~7.8 ppm are assigned to the –CH and –NH in the PAZ segement, respectively. The main structure of the chitosan segment can be confirmed owing to the presence of the peaks at ~3.4 ppm, ~3.75 ppm and ~4.9 ppm. According to the ^{1}H NMR spectra, we determined the degrees of substitution of FA and TK (i.e., degree of CS functionality for FA and TK) were 19% and 10%, respectively. In addition, since the degree of substitution means the number of FA segment grafting onto the CS backbone (i.e., degree of substitution), the molar ratio of FA/CS is 0.19:1. Similarly, the molar ratio of FA/TK is 2:1. The chemical composition of CS-FTP was analyzed using Fourier transform infrared spectroscopy (FTIR) (Fig. 1d). The bands highlighted in Fig. 1d confirm the presence of the FA unit (in berry red shade: at 1520 cm^{-1} and 1630 cm^{-1} are ascribed to the amide I and amide II, respectively, in yellow green shade: at 3500 cm^{-1} is ascribed to the phenolic hydroxyl group from FA) and TK linker (in orange shade: at 650 cm^{-1} is attributed to the vibration of C–S from TK) on the CS backbone (in dark cyan shade: at 2990 cm^{-1} is associated with the C–H stretching from CS). Moreover, the increase in intensity of the band at 1250 cm^{-1} (in blue shade), is associated with S═O stretching characteristic of PAZ, confirming the graft of PAZ to the modified CS [43,44].

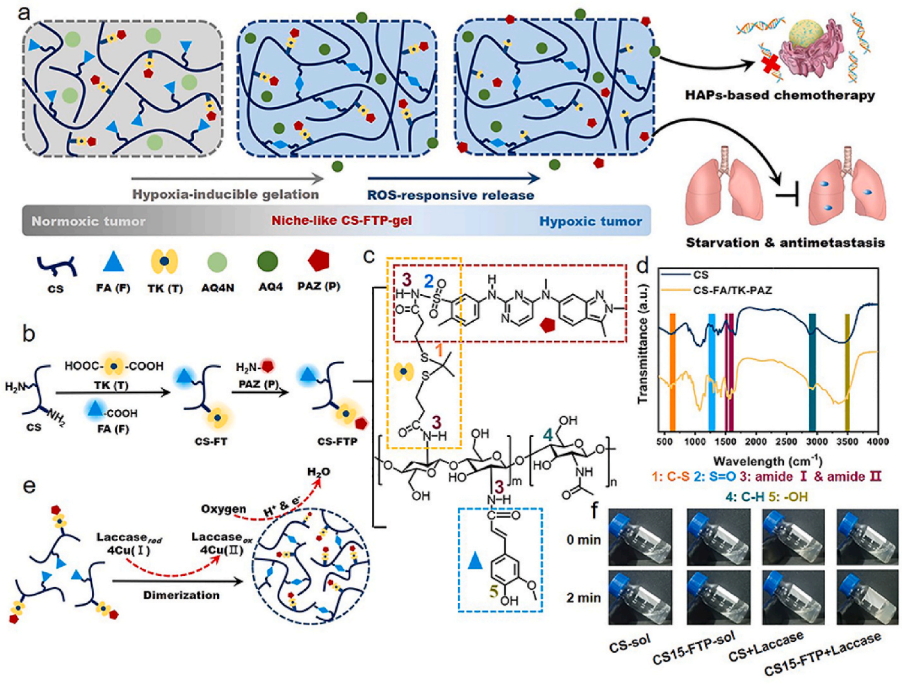

Fig. 1. Design CS-FTP-gel. (a) Schematic of combination antitumor therapy using niche-like CS-FTP-gel. (b) Synthesis of CS-FTP polymer. (c) Chemical structure of CS-FTP. Functional moieties conjugated to CS backbone are indicated with dotted boxes of different colors. (d) FTIR spectra of CS and CS-FA/TK-PAZ (CS-FTP). (e) Schematic representation of CS-FTP-gel formation. CS-FTP-gel is formed via laccase-mediated dimerization of FA molecules with oxygen consumption. Laccase catalyzes the four-electron reduction of oxygen to water molecules, resulting in oxidation of FA to form diferulic acid (DiFA) and crosslinking of polymer network. (f) Phase transitions of CS solution (CS-sol, 3 wt%) and CS-FTP solution (CS-FTP-sol, 3 wt%) with/without addition of laccase (25 U ml^{-1}).

2.2. Formulation and characterizations of CS-FTP-gel

The CS-FTP-gel was fabricated by laccase-mediated reaction (Fig. 1e and Fig. S2), a reaction that has been widely used in food chemistry and biosensors [45]. In a typical preparation process, the CS-FTP undergo gelation by crosslinking FA molecules via laccase-mediated dimerization to form DiFA, which consumes oxygen and yields polymer networks. As verified by inversion test (Fig. 1f and Fig. S3), the hydrogels formed within 120 s after simply mixing laccase with CS15-FTP polymer solution (namely CS15-FTP-sol, and CS molecular weight was 150 kDa). Furthermore, the degradation of the hydrogels was tested. The formed hydrogel was immersed in saline and the dry mass of hydrogel was measured at set intervals. Fig. S4 shows the mass change as a function of time, which reveals that the hydrogel degraded completely within six days. To study whether molecular weight of CS has an effect on hydrogel structure and performance, we synthesized CS-FTP polymer with various CS molecular weights (i.e., 100 kDa, 150 kDa, and 400 kDa) and named them as CS10-FTP, CS15-FTP, and CS40-FTP, respectively. As shown in Fig. 2a, the morphology with porous structure of the hydrogel network was observed by scanning electron microscopy (SEM). The SEM images indicate that CS10-FTP-gel and CS15-FTP-gel have similar porosity and pore size, in contrast, the CS40-FTP-gel shows more compact with obviously diminished porosity, which is considered to be related to the different molecular weights of CS [46]. As molecular weight dramatically increases, the hydrophilicity of CS will become poor so that the gel formed from CS40 contain less free water, resulting in reduced porosity after lyophilization process for SEM imaging.

Afterwards, the gelation time observed by phase transition and the oxygen-consuming ability of CS-FTP polymer during hydrogel formation were investigated. In inversion test, we recognized the time point when phase transition occurred as gelation time shown in Fig. 2b and c. It is found that higher concentrations of laccase or polymer induce faster hydrogel formation. To determine oxygen levels within the matrix, we monitored dissolved oxygen (DO) levels at the bottom of hydrogels using a noninvasive sensor patch [47]. In comparison with solution of laccase or CS-FTP, the DO level of mixed solution of laccase and CS-FTP was decreased, demonstrating that laccase-mediated gelation could induce rapid oxygen consumption and low oxygen levels (Fig. 2d). In brief, a novel kind of oxygen-consuming hydrogels with tunable gelation time essential for injection window has been successfully constructed.

To further test the hydrogel formation and viscoelastic modulus, the rheological analysis, including dynamic time sweep of hydrogels with varying CS molecular weights was conducted (Fig. S5 and Fig. 2e–g). It should be noted that the same concentration of FA molecule was used to maintain the same FA feed amount in all samples examined. The crosslink point (gel points) of elastic (G') and viscous (G'') modulus, which provides an estimate of the gelation time (arrows in Fig. S5 and Fig. 2e), occurs within 0.5–10 min, in agreement with the gelation kinetics observed by phase transition (3 wt% polymer, 25 U ml^{-1} laccase), indicating that CS molecular weight affects the network formation kinetics. According to Fig. 2f, the final elastic moduli of the CS40-FTP-gel (800 ± 1.2 Pa) were markedly higher than that of the CS15-FTP-gel (62.5 ± 5.9 Pa) and CS10-FTP-gel (80.9 ± 6.8 Pa), suggesting that mechanical properties are dependent on CS molecular weight. The faster gelation and higher elastic modulus of hydrogel with high CS molecular weight can be attributed to the physical gelation behavior, in which hydrogel of high molecular weight retained more amine and hydroxyl groups to facilitate hydrogen bonds-induced physical crosslinking [48]. In addition, all the values of tan δ (= G''/G'), a signature of elastic behavior of hydrogel, were less than 1.0 for all three hydrogels, confirming that aforementioned hydrogels were crosslinked gels (Fig. 2g) [49]. By using visual blue dye [50], we further confirmed the gelation behavior and distribution of CS-FTP-gel within tumor. Alcian blue were loaded into the CS-FTP-gel for visualization and the tumor injected by CS-FTP-sol/laccase mixture was dissected to observe the mixture state. As shown in Fig. S6, the formation of CS-FTP-gel within tumor could be performed and the blue dye spreading to the whole cross section was observed, confirming the homogenous distribution of CS-FTP-gel inside tumor. In brief, all of three CS-FTP polymers with different CS molecular weight (100 kDa, 150 kDa, and 400 kDa) could form the crosslinked gel and the molecular weight of CS could cause major mechanical property changes.

The drug release profiles of CS-FTP-gel was then studied. The tumor vascular system that enhances the distribution and penetration of drugs plays a critical role in the drug delivery to tumor cells [51]. In the CS-FTP-gel, AQ4N was encapsulated physically so that they could

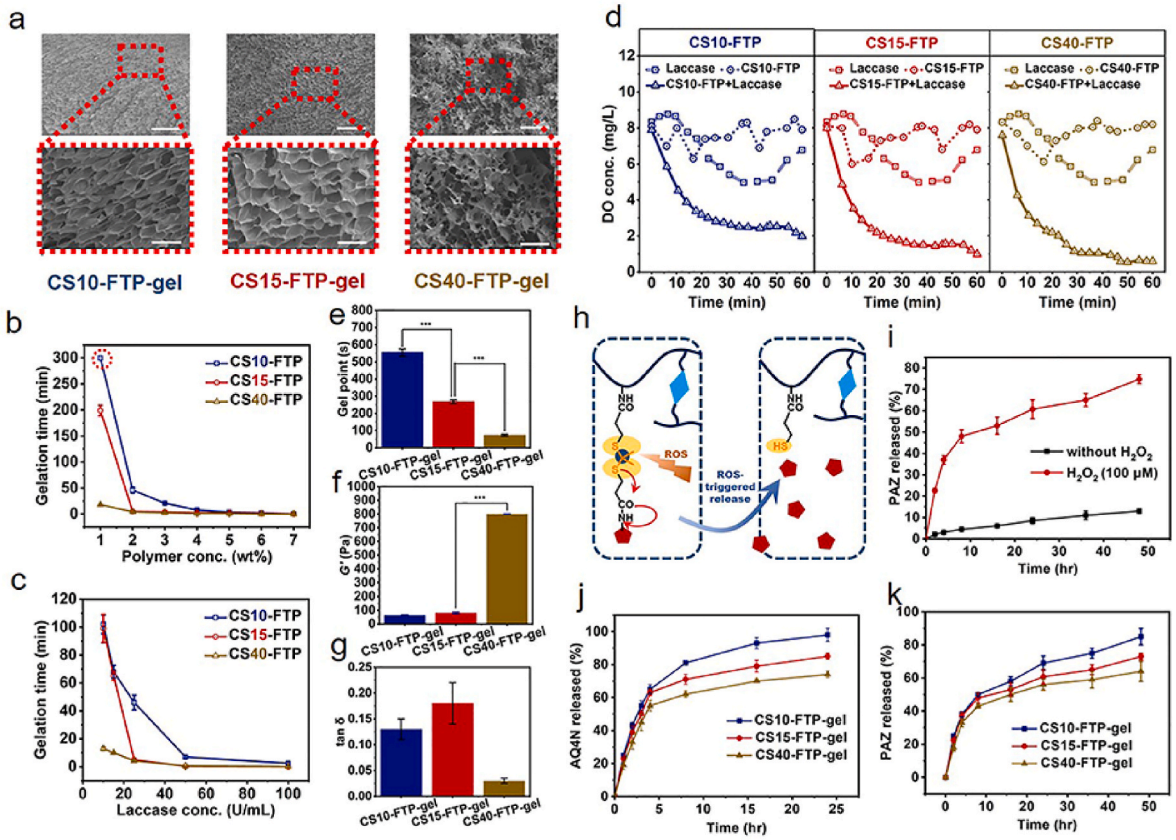

Fig. 2. Hydrogel formation kinetics and characterizations of CS-FTP-gel. (a) Representative SEM images of hydrogel scaffolds with different CS molecular weights (blue: CS10-FTP-gel, red: CS15-FTP-gel, dark yellow: CS40-FTP-gel). Scale bars, 250 μm. Dotted boxes: zoomed-in images of the scaffolds. Scale bars, 50 μm. Effect of (b) polymer concentration (laccase concentration of 25 U mL^{-1}, red dotted circle represents points that fails to gelation) and (c) laccase concentration (polymer concentration of 3 wt%) on gelation time. (d) Measured DO levels in solutions of laccase, solutions of CS-FTP polymer, mixed solutions of laccase and CS-FTP polymer (3 wt% polymer, 25 U ml^{-1} laccase). Statistical analysis of (e) gel points, (f) final storage moduli, and (g) tan δ of the CS10-FTP-gel, CS15-FTP-gel, and CS40-FTP-gel. (h) Proposed mechanism for the activation of PAZ. (i) Release profiles of PAZ from CS15-FTP-gel incubated in phosphate-buffered saline (PBS) buffer (pH 7.4) with or without 100 μM H_2O_2. (j) Release profiles of AQ4N from CS10-FTP-gel, CS15-FTP-gel, and CS40-FTP-gel, respectively. (k) Release profiles of PAZ from CS10-FTP-gel, CS15-FTP-gel, and CS40-FTP-gel, respectively. $n = 3$, mean ± s. d. $^*P < 0.05$, $^{**}P < 0.01$, $^{***}P < 0.001$.

release from hydrogel quickly to diffuse into tumor cells through tumor vessel. To ensure the mature of tumor vessel for sufficient distribution of AQ4N inside tumor, the release profile of antiangiogenic PAZ should be much slower. To this end, we designed a ROS-responsive sustained-release pattern to postpone the antiangiogenesis effect, thus contributing to the improvement of intratumor distribution of AQ4N. As shown in Fig. 1a, PAZ was conjugated to the CS backbone and the AQ4N was physically encapsulated into polymer network during sol-gel transition, respectively. Fig. 2h illustrates the correlated mechanism of ROS-activation of PAZ. Tumorous redox homeostasis generated overexpressed ROS that efficiently cut the ROS-cleavable linker (i.e., TK) via oxidation to induce the release of short thiol ligand caged PAZ. The caged PAZ then underwent a well-known self-immolation via intramolecular nucleophilic acyl substitution on the amido moiety to form free PAZ [52]. To verify the ROS-responsive release of PAZ, hydrogel samples were immersed in PBS containing 100 μM H_2O_2 at 37 °C. The release behaviors of PAZ and AQ4N were quantified using UV spectroscopy. As expected, PAZ was released from hydrogel in H_2O_2 solution with an increased rate compared to that in PBS only (Fig. 2i). Moreover, both of PAZ and AQ4N showed CS molecular weight-dependent release profiles, suggesting that compact hydrogel network could restrict diffusion behavior of drugs (Fig. 2j and k).

2.3. *In vitro* therapeutic effect of hypoxia-inducible CS-FTP-gel

Inspired by the oxygen-consuming performance and ROS-responsive drug release of the hydrogels we further postulated that CS-FTP-gel could remodel tumor hypoxic environments and enhance cytotoxicity *in vitro*. Towards this, we first imaged DO levels in culture media of 4T1 cells using oxygen sensor foils [53]. As depicted in Fig. 3a, the detecting camera captures the DO-dependent fluorescence generated from oxygen sensor to image and determine DO levels. In a typical protocol, PBS, laccase solution, CS-FTP polymer solution or CS-FTP/laccase mixed solution were added into the culture after cell seeding. In comparison with solutions (PBS, laccase, and three CS-FTP-sols), CS-FTP/laccase mixed solution could gelate in the cell culture and consume oxygen efficiently (Fig. 3b). More specifically, the DO concentration of CS-FTP-gel-treated cell dramatically decreased to less than 1.5 mg L^{-1}, affirming that gelation of CS-FTP polymer could enhance hypoxic environment of cell (Fig. 3c). The CS-FTP-gel-mediated cellular oxygen scavenging in 4T1 cells was also verified by the fluorescence microplate reader using an aromatic compound with nitroreductase-sensitive nitro unit as a hypoxia detection. As shown in Fig. 3d and Fig. S7, cells treated with CS-FTP polymer solutions display no difference in fluorescent intensity as compared with control group (PBS), whereas obviously increased fluorescent intensity were detected in cells treated with CS-FTP-gels.

To determine whether molecular weight of CS would affect cell viability, we assessed cytotoxicity with 4T1 cells cultured in hydrogel extractions. As shown in Fig. S8, 4T1 cells treated with laccase showed concentration-dependent declines. 4T1 cells treated with laccase of 25 U mL^{-1} and 50 U mL^{-1} showed negligible cytotoxicity, while laccase of

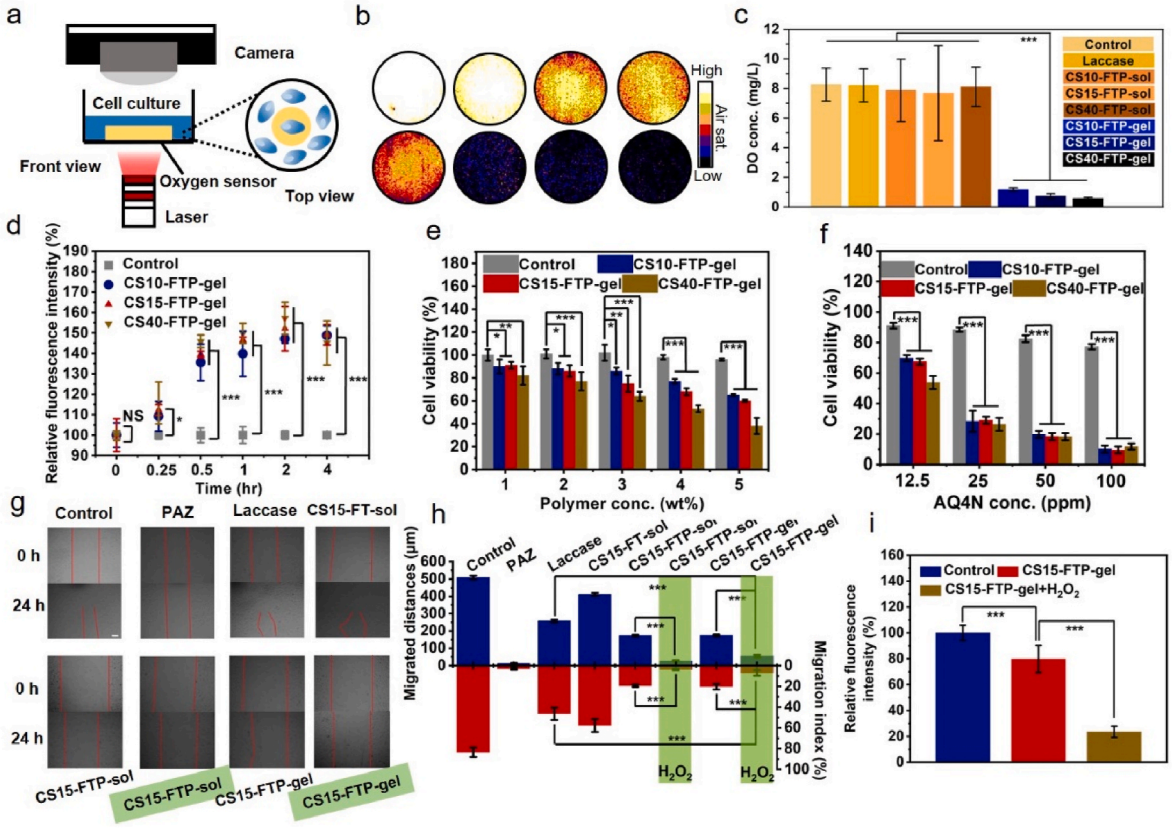

Fig. 3. The performances of CS-FTP-gel in cellular level. (a) Schematic presentation for detecting DO in cell culture. (b) DO level imaging in culture plates with different addition (first row: from left to right, PBS, laccase solution, CS10-FTP-sol, CS15-FTP-sol, respectively. second row: from left to right, CS40-FTP-sol, CS10-FTP-gel, CS15-FTP-gel, CS40-FTP-gel, respectively). (c) DO concentrations determined from (b). $n = 3$, mean ± s. d. (d) The effect of CS-FTP-gel on hypoxia level in 4T1 cells. $n = 3$, mean ± s. d. *In vitro* cytotoxicity of 4T1 cells with various polymer concentrations (e) and various AQ4N concentrations (f). $n = 4$, mean ± s. d. (g) Inhibitory effect of bEnd.3 cells migration (PAZ: 5 mg mL^{-1}, laccase: 25 U mL^{-1}, CS15-FT-sol: 3 wt%, CS15-FTP-sol: 3 wt%, CS15-FTP-sol with green shade: 3 wt% with addition of 100 μM H_2O_2, CS15-FTP-gel: hydrogel formed from mixed solution of 3 wt% CS15-FTP and 25 U mL^{-1} laccase was immersed in PBS to generate extraction, CS15-FTP-gel with green shade: hydrogel formed from mixed solution of 3 wt% CS15-FTP and 25 U mL^{-1} laccase was immersed in PBS with addition of 100 μM H_2O_2 to generate extraction). Scale bar, 100 μm. (h) Migration distances and migration index measured from (h). $n = 3$, mean ± s. d. (i) The effect of CS15-FTP-gel on VEGFR1 levels. $^*P < 0.05$, $^{**}P < 0.01$, $^{***}P < 0.001$. NS represented no significance.

100 U mL^{-1} and 200 U mL^{-1} caused significant cell damage. Given that too fast gelation kinetics will hamper the expansion of CS-FTP-gel inside tumor and cause needle blocking, we chose 25 U mL^{-1} (gelation time was around 3 min) rather than 50 U mL^{-1} (gelation time was less than 1 min) (Fig. 2c). It is also found that all three hydrogels display increased cytotoxicity as polymer concentration for gelation improved (Fig. 3e). Thus, we should choose low concentration to prepare polymer solutions. However, gelation kinetics decreased dramatically (gelation time was more than 5 min) as polymer concentration reduced to 2 wt% or less, which might limit the retention of CS-FTP-gel inside tumor (Fig. 2b). All things considered, we thus chose polymer concentration of 3 wt% and laccase concentration of 25 U mL^{-1} for comprehensive comparison. Notably, hydrogel consisting of high-molecular-weight chitosan (400 kDa) exhibited extremely poor cell compatibility with low cell viability less than 60% when polymer concentrations exceeded 3 wt%. Chitosan with positive charged amino groups could bind to cells with negative charge, disrupting the cell membranes through electrostatic interaction and thus damaging the cells [54,55]. Therefore, the higher the molecular weight of chitosan, the more the positive amino groups, the stronger its cytotoxicity. Moreover, CS-FTP-gel loaded with AQ4N showed further enhanced cytotoxicity due to the improved hypoxic environment of cells caused by CS-FTP-gel, indicating that AQ4N as a HAP could exert potent antitumor efficacy under hypoxic condition (Fig. 3f). Besides, migration and invasion of endothelial cells are essential in angiogenesis, which can be inhibited by blocking the expression of vascular endothelial growth factor receptor (VEGFR) family with PAZ. Therefore, we further tested antiangiogenic activity of CS-FTP-gel by establishing an *in vitro* wound healing model based on mouse brain endothelial cells (bEnd.3) (Fig. 3g). For hydrogels, we still used extractions to treat cells. It is found that cells treated with PBS, laccase, CS15-FT-sol, that is, no addition of PAZ, show significant recovery of the wounded monolayer, while the scratched monolayers treated with CS15-FTP or CS15-FTP-gel extractions display sizable wound area. In particular, the addition of H_2O_2 into CS15-FTP-sol group or CS15-FTP-gel group could further inhibit the migration of cells, which resulted in obviously decreased migration index comparable to that of free PAZ-treated cells, implying that ROS-cleavable CS15-FTP polymer could enhance antiangiogenesis by releasing PAZ (Fig. 3h). Furthermore, a probe based on anti-flk-1 primary antibody and Alexafluor 568 goat anti-rabbit IgG secondary antibody was employed to observe the changes of cellular VEGFR1/-VEGFR2 levels. In comparison with control group, CS-FTP-gel extraction-treated cells expressed less VEGFR1/VEGFR2, suggesting that fractions of hydrogels might degrade into extract media to block the receptors. With the addition of H_2O_2, the hydrogels could release PAZ into medium thus further inhibiting the expression of VEGFR1/VEGFR2 (Fig. 3i and Fig. S9). In addition, the gelation kinetics of CS10-FTP with 25 U mL^{-1} laccase were too slow to form hydrogel inside tumor, limiting the retention of CS10-gel in lesion site. By contrast, the gelation kinetics of CS15-FTP were much more appropriate for *in situ* hydrogel formation inside tumor. Therefore, CS15-FTP-gel was chosen to conduct *in vivo*

experiments due to its fast gelation and good cell compatibility. All the above results demonstrated that molecular weight of CS could affect the hydrogel performances including mechanical properties, drug release, and cytotoxicity.

2.4. In vivo distribution and deoxygenation performance of CS15-FTP-gel

Motivated by the interesting oxygen depletion results *in vitro*, we further studied the CS15-FTP-gel performance *in vivo*. To verify the retention ability of the hydrogel, 4T1 tumor-bearing mice model was established. For whole body fluorescence imaging, the cyanine dye Sulfo-Cyanine7 (cy7) was encapsulated into CS15-FT-gel, yielding CS15-FT-gel@cy7. Meanwhile, free cy7 and CS15-FT-gel@cy7 were intratumorally injected respectively, for comparison. The fluorescence signal remained detectable five days after gel injection, while there is nearly no signal for the groups of free Cy7, indicating that encapsulation of drug in gel can increase its retention in the tumor sites (Fig. 4a). Furthermore, the immunofluorescence and PET/CT imaging were used to reveal the oxygen depletion of hydrogel *in vivo*. It is clearly found that compared with control (G1 and G4), the immunofluorescence of hypoxia in tumor area were intensified when CS15-FTP-gel (G3 and G6) or CS-15-FT-gel (G2 and G5) administration were achieved, in which the expression of hypoxia inducible factor-1 alpha (HIF-1α) were upregulated (Fig. 4b), suggesting that CS15-FT polymer could induce tumor hypoxia during gelation even without assistance of antiangiogenic Pazopanib (P). Afterwards, we assessed the prohypoxia potential of the hydrogels using micro-PET imaging measurement. The ^{18}F-fluoromisonidazole (^{18}FMISO) was chosen as the probe, since as an oxygen-susceptible molecule, ^{18}FMISO could only stably exist under hypoxic condition, making it a sensitive label for monitoring hypoxia [57]. Fig. 4c and Fig. S10 show the 3D PET/CT images and the strongest signal of ^{18}FMISO can be observed in the mouse treated with CS15-FT-gel, confirming the severe hypoxic condition within the tumor after oxygen-consuming gelation. It is worth noting that accumulation of ^{18}FMISO in tumors treated with CS15-FTP-gel is barely noticeable, suggesting that ^{18}FMISO probes administrated by intravenously injection are difficult to uptake into tumor tissue due to the PAZ-mediated antiangiogenesis, which was also supported by the relative standardized uptake values (relative SUVmax) of the regions of interest (Fig. 4d). More details, it is found that the situation of hypoxia in mice treated with CS15-FT-gel grown to be significantly worse (SUV: 6.5 ± 1.71) than that of mice in control, CS15-FT-sol, and laccase group. Consistently, the decreased content of standardized uptake was also witnessed in mice receiving CS15-FTP-gel (SUV: 1.76 ± 0.23). Thus, we concluded that CS15-FTP-gel treatment not only could enhance the tumor hypoxia but efficiently inhibit angiogenesis within tumor for starvation therapy and antimetastasis.

2.5. In vivo therapeutic performance of CS15-FTP-gel@AQ4N

Finally, the 4T1 mouse breast tumor model was established to validate whether the proposed combination chemo-starvation therapy strategy can promote antitumor effects. Tumor-bearing mice were injected intratumorally with PBS (200 μL per mouse), CS15-FT-gel (200 μL per mouse), CS15-FTP-gel (200 μL per mouse), HA@AQ4N (200 μL per mouse), CS15-FT-gel@AQ4N (200 μL per mouse) or CS15-FTp-gel@AQ4N (200 μL per mouse). In addition, a reference hyaluronic acid hydrogel loaded with AQ4N (i.e., HA@AQ4N, no hypoxia-enhanced effect) was prepared to provide chemotherapeutic outcome of AQ4N mediated by a non-prohypoxic hydrogel for comparison. These mice were administered at the very first day, and then the tumors were monitored for 14 days (Fig. 5a). During 14 days, no abnormal behaviors or significant weight loss were observed (Fig. 5d). The empty hydrogel (CS15-FT-gel) and HA@AQ4N groups showed similar effects and were not superior to untreated control, indicating that AQ4N failed to inhibit tumor growth without prohypoxia condition. Group of CS15-FTP-gel or CS15-FT-gel@AQ4N-treated mice showed a delay of tumor growth, suggesting a slight inhibitory of single treatment based on either AQ4N-dependent chemotherapy with enhanced tumor hypoxia or PAZ-mediated starvation therapy. Particularly, mice receiving CS15-FTP-gel@AQ4N showed noticeable tumor inhibitory rates of 63.98%, confirming the therapeutic efficacy of combination of AQ4N and PAZ to elicit chemo-starvation (Fig. 5b, c, 5e and 5f). Survival profiles shown in Fig. 5g indicated that mice of 40% survived at least 60 days after receiving CS15-FTP-gel@AQ4N, whereas none of the mice survived in any of the control groups exceed to 2 months. After the terminal of therapeutic experiments, the excised tumors were sliced for histological examination. Hematoxylin and eosin (H&E) staining (Fig. 5h) and terminal deoxynucleotidyl transferase dUTP nick end labeling (TUNEL) staining (Fig. S11) showed that CS15-FTP-gel@AQ4N caused the highest degree of damage compared to other groups. Furthermore, to optimize the administration scheme of the hydrogel, the CS15-FTP-gel@AQ4N were injected on day 1 and day 5 to achieve two-stage treatment (Fig. 5i). By sharp contrast, persistent regression of tumors was observed in such two-stage treatment group (Fig. 5j–l and Fig. S12), indicating that the therapeutic effect can be significantly improved by adjusting the administration regimen. Additionally, biocompatibility of the CS15-FTP-gel was also assessed after the therapeutic experiment. At the end of investigation, the major organs of the treated mice were subjected to histological examination, which did not signal any overt damage,

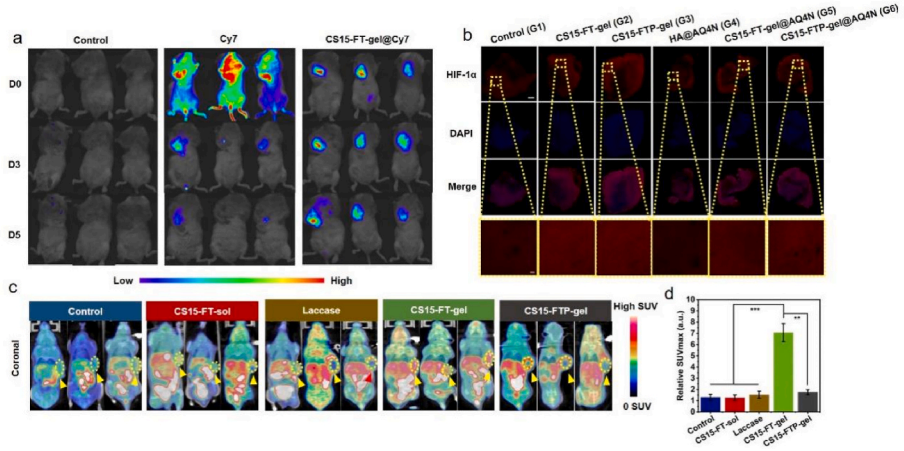

Fig. 4. Characterizations of *in vivo* retention and deoxygenation performance. (a) Whole body fluorescence imaging of 4T1 tumor-bearing mice administrated with saline (control), cy7 (1 mg kg^{-1}) or CS15-FT-gel@cy7 (3 wt% CS15-FTP, 25 U mL^{-1} laccase, 1 mg kg^{-1} cy7 and injection dose was 200 μL). (b) Immunofluorescence images of tumor slices stained by HIF-1α (red) after intravenous injection of saline (control), CS15-FT-gel, CS15-FTP-gel, HA@AQ4N, CS15-FT-gel@ AQ4N, or CS15-FTP-gel@ AQ4N. Scale bar, 1000 μm. Dotted boxes: zoomed-in images. Scale bar, 100 μm (c) ^{18}FMISO micro-PET/CT images of mice received different treatments (saline, CS15-FT-sol: 3 wt%, laccase: 25 U mL^{-1}, CS15-FT-gel: mixed solution of 3 wt% CS15-FT and 25 U mL^{-1} laccase, CS15-FTP-gel: mixed solution of 3 wt% CS15-FTP and 25 U mL^{-1} laccase, injection dose of all five groups: 200 μL). (d) Relative SUVmax profiles. The images were captured at 1 h post i.v. injection of ^{18}FMISO probe. $n = 3$, mean ± s. d. $^{*}P < 0.05$, $^{**}P < 0.01$, $^{***}P < 0.001$.

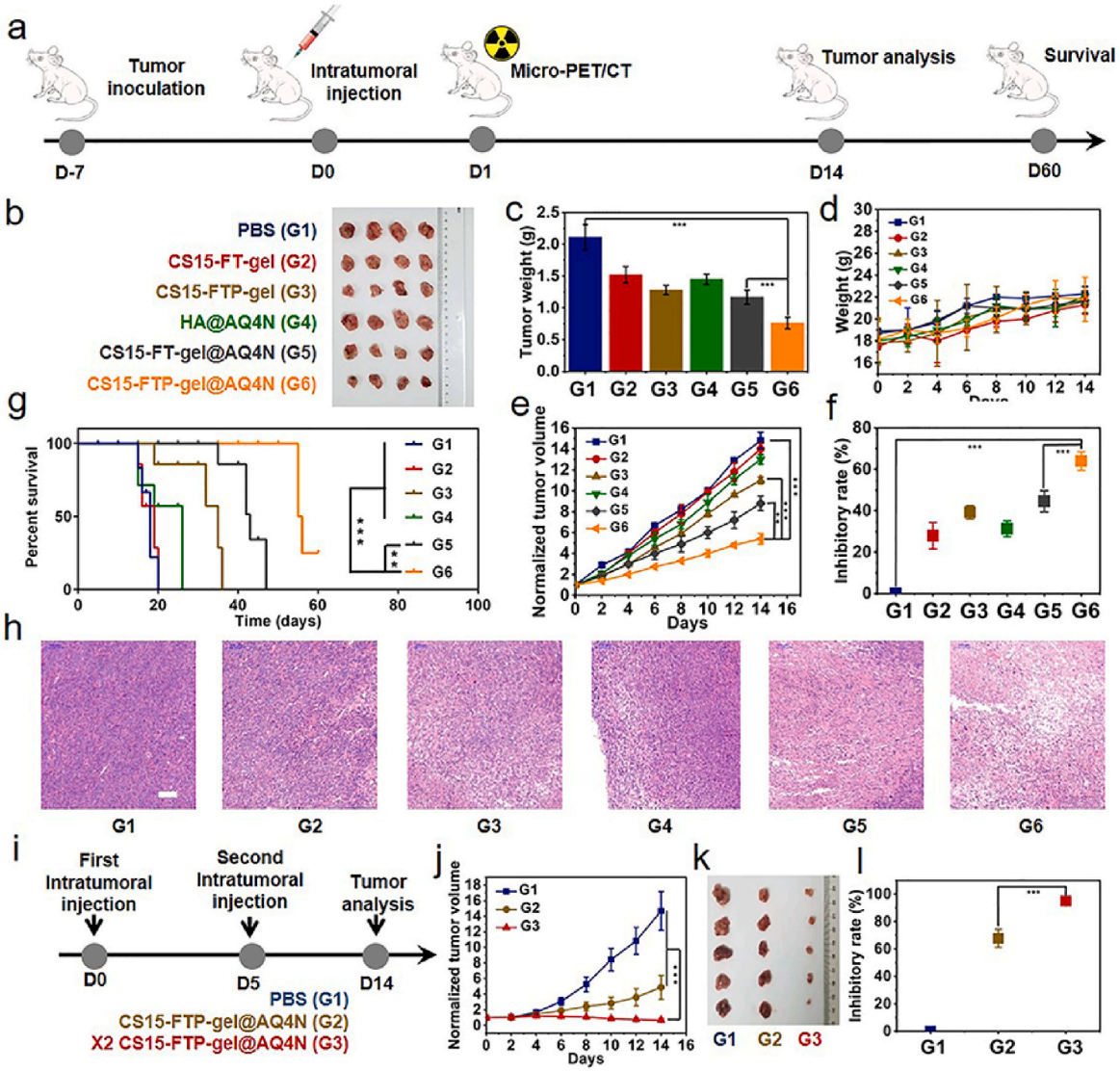

Fig. 5. ***In vivo*** **evaluations of therapeutic outcome.** (a) Schematic of the treatment regimen. (b) Digital images of the 4T1 tumors of the mice treatment with different samples at day 14 (G1: PBS, G2: mixed solution of 3 wt% CS15-FT and 25 U mL^{-1} laccase, G3: mixed solution of 3 wt% CS15-FTP and 25 U mL^{-1} laccase, G4: 100 mg mL^{-1} HA and 1 mg mL^{-1}AQ4N, G5: mixed solution of 3 wt% CS15-FT and 25 U mL^{-1} laccase, 1 mg mL^{-1}AQ4N, G6: mixed solution of 3 wt% CS15-FTP and 25 U mL^{-1} laccase, 1 mg mL^{-1}AQ4N). (c) Tumor weight within 14 days. (d) Body weight change curves. (e) Tumor growth curves. (f) Tumor growth inhibitory rates. (g) Survival curves for the treated and control mice. (h) Histological observation of the tumor tissues. The tumor sections were stained with H&E. Scale bar, 100 μm. (i) Schematic of the two-stage treatment regimen. (j) Tumor growth curves. (k) Digital images of the 4T1 tumors of the mice treatment with different samples at day 14. (l) Tumor growth inhibitory rates. $n = 5$, mean ± s. d. $^{*}P < 0.05$, $^{**}P < 0.01$, $^{***}P < 0.001$.

confirming the biosafety of these treatment. (Fig. S13). Together, all the *in vivo* results support that CS15-FTP-gel@AQ4N treatment, especially with two-stage administration will trigger a robust chemo-starvation therapy against tumor growth.

Furthermore, vessel density (blood and lymphatic vessel) and VEGFR (VEGFR1 and VEGFR3) signaling in the tumor region were examined to confirm the antitumor mechanism of combination therapy. Compared with the PBS group, the tumors treated with CS15-FT-gel showed an obviously higher blood vessel density (visualized by anti-CD31 immunohistochemistry) and VEGFR1 expression due to the hypoxia-induced angiogenesis [56]. Interestingly, PAZ-containing hydrogel, namely CS15-FTP-gel@AQ4N, significantly reduced the vessel density and VEGFR levels in tumor tissue (Fig. 6a–e and Figs. S14–S15), indicating that PAZ notably neutralized the strong angiogenic tumoral response to tumor hypoxia and contributed to the enhancement of above-mentioned combinatory cancer therapy. The role of angiogenesis in tumor growth has been studied continuously for several decades. It is now appreciated that angiogenesis is essential for the dissemination and establishment of tumor metastases. In tumor progression, angiogenesis is a necessity for the escape of tumor cells into the bloodstream and for the establishment of metastatic colonies in secondary sites [58]. In addition, the tumor lymphangiogenesis is also important as a means of dissemination of lymphatic metastases [59]. Thus, as an antiangiogenic agent, PAZ could prevent tumor metastasis via antiangiogenesis pathway and collaborate with the hypoxia-inducible hydrogel for optimization of HAP-based chemotherapy. Encouraged by the *in vivo* therapeutic outcome, we further evaluated antimetastasis ability of CS15-FTP-gel@AQ4N on an orthotopic 4T1 breast tumor model. Orthotopic breast cancer-bearing mice in every group were administrated with two-stage procedure (Fig. 6f). As shown in Fig. 6g and Figs. S16–S17, without AQ4N and PAZ, the tumor of CS15-FT-gel-injected mice grew as fast as those of PBS-injected mice, while the growth of tumors for CS15-FT-gel@AQ4N-treared mice was partially inhibited owing to the chemotoxicity of AQ4N under tumor hypoxia. In sharp contrast, the

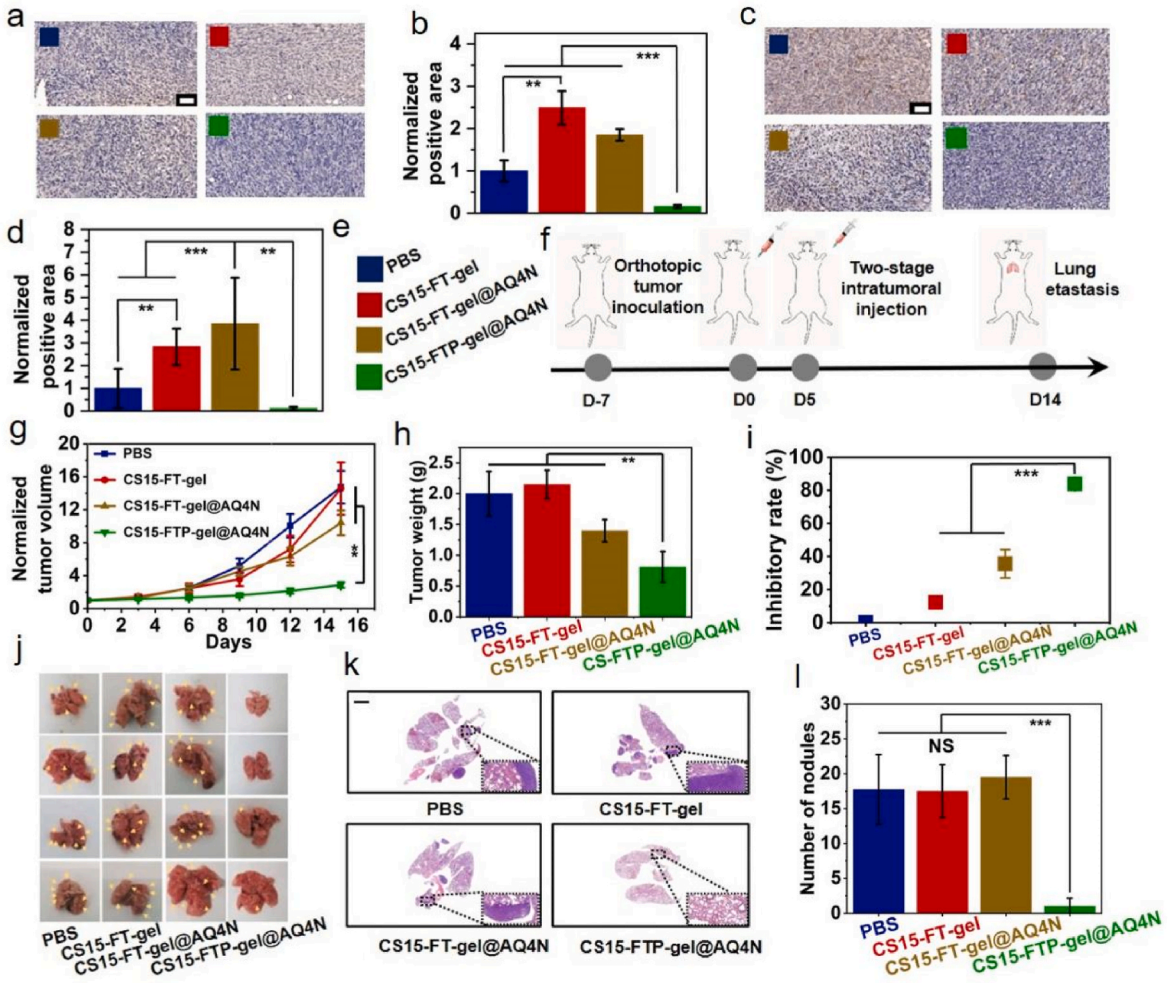

Fig. 6. ***In vivo*** **evaluations of antimetastasis.** (a) Representative tumor sections from different treatment groups with immunostaining for VEGFR1. Scale bar, 100 μm. (b) Quantitative analysis for positive area of results in (a). (c) Histological analysis showing representative tumor sections from different treatment groups stained for CD31. Scale bar, 100 μm. (d) The corresponding quantitative analysis for positive area of results in (c). (e) Samples in different groups (blue: PBS, red: mixed solution of 3 wt% CS15-FT and 25 U mL^{-1} laccase, dark yellow: mixed solution of 3 wt% CS15-FT and 25 U mL^{-1} laccase, 1 mg mL^{-1}AQ4N, green: mixed solution of 3 wt% CS15-FTP and 25 U mL^{-1} laccase, 1 mg mL^{-1}AQ4N). (f) Schematic of the treatment regimen for lung metastasis. (g) Normalized tumor growth curves. (h) Tumor weight within 14 days. (i) Tumor growth inhibitory rates. $n = 5$, mean ± s. d. (j) Lung photographs of lung metastasis nodules in different groups. (k) Representative H&E-images of lung tissues in different groups. Scale bar, 2000 μm. The inset were the zoomed-in images. Scale bar, 100 μm. (l) Number of lung metastasis nodules in different groups. $n = 4$, mean ± s. d. $^*P < 0.05$, $^{**}P < 0.01$, $^{***}P < 0.001$. NS represented no significance.

CS15-FTP-gel@AQ4N-injected mice showed the smallest tumor volume after 14 days with an excellent inhibitory rate as high as 83.88% (Fig. 6h and i). Such a greatly enhanced tumor inhibitory effect of CS15-FTP-gel@AQ4N should be attributed to the synergistic action of AQ4N-based chemotherapy and PAZ-based starvation. It is known that tumor blood and lymphatic vessel growth are the key factor for tumor hematogenous metastasis [60]. In this study, as we mentioned above, PAZ released due to the exposure of hydrogel to the overexpressed ROS within tumor to specifically block the expression of VEGFR family that are associated with vascular growth would be expected to inhibit the blood/lymphatic vascular growth for mitigating tumor hematogenous metastasis. Thus, lungs of mice after therapy were extracted for histological analysis and metastatic nodule counting to verify the antimetastasis effect of CS15-FTP-gel@AQ4N (Fig. 6j–l). As shown in H&E staining images, no tumor metastasis was observed in the lungs of mice after CS15-FTP-gel@AQ4N -mediated therapy, while metastatic tumors distributed in the lungs of mice after the other treatments. More than 15 metastatic nodules were observed in each lung of the PBS-injected control mice, CS15-FT-gel-injected mice and CS15-FT-gel@AQ4N-injected mice, while the average number of pulmonary metastasis nodules in CS15-FTP-gel@AQ4N-treated mice was 1.0. These results demonstrated that CS15-FTP-gel@AQ4N could efficiently inhibit the cancer lung metastasis with the synergy of PAZ. In brief, the *in situ* formation of oxygen/ROS-responsive niche-like hydrogel CS15-FTP-gel@AQ4N, as well as its mediated cancer therapy in this work not only remarkably suppressed tumors, but also inhibited lung metastasis.

3. Conclusions

In summary, a novel hypoxia-inducible hydrogel CS15-FTP-gel@AQ4N was developed, which endows with a ROS-activatable pharmacological profile for metastasis-inhibited chemo-starvation combination cancer therapy. Impressively, this niche-like hydrogel was achieved *in situ* using mixed solution of CS15-FTP polymer and laccase via intratumorally injection, which is aimed at remodeling tumor hypoxic microenvironment and developing hypoxia-based chemotherapy. More specifically, after injection into tumor region, the mixed solution could perform oxygen-consumable dimerization and thus undergo gelation within 3 min, leading to an enhanced tumor hypoxia condition which favors for activation of AQ4N-to-AQ4 toxicity to maximize chemotherapeutic efficacy. Moreover, antiangiogenic PAZ conjugated

onto CS backbone of the polymer via ROS-sensitive linker could be released by overexpressed ROS in tumor and serve as an efficient agent for tumor starvation. More importantly, a significantly inhibition of metastasis for 4T1 tumor was observed by the PAZ-mediated anti-antiangiogenesis, providing a positive indicator that hypoxia-induced cancer metastasis could be mitigated. Overall, this research offers a smart design to compact solutions for multiple obstacles in hypoxia-based cancer therapy into a concise formulation, which, as we believe this niche-like hydrogel and its combinatory strategy will hold promise to further clinical translation and would have major implications for the field of antitumor therapy.

4. Materials and methods

Cell lines: 4T1 cell line and bEnd.3 cells were maintained at 37 °C under 5% CO_2 in high-glucose DMEM (Auxgene), supplemented with 10% heat-inactivated fetal bovine serum, streptomycin (100 mg mL^{-1}) and penicillin (100 units mL^{-1}). All the cell lines were acquired from Shanghai Institute of Biochemistry and Cell Biology, Chinese Academy of sciences.

Animal experiment: BALB/c nude mice (6 weeks, female) were purchased from Beijing Vital River Laboratory Animal Technology Co. All experimental protocols were complied with the policies of the National Ministry of Health and care regulations approved by the administrative committee of laboratory animals of Fudan University.

Synthesis of TK: 3-Mercaptopropionic acid (5.2 g) and anhydrous acetone (5.8 g) were dissolved in dry hydrogen chloride and stirred at room temperature for 6 h. The reaction was further quenched by placing the mixture on ice until the crystallization was complete. After filtration, the filtrate was washed by hexane and cold water, and the product was dried. ^{1}H NMR spectra was recorded on a Bruker Ascend 500 spectrometer with DMSO-d_6 as the solvent. ^{1}H NMR (DMSO-d_6, 500 MHz, δ ppm): 3.45 (dd, 2H), 2.75 (d, 2H), 1.53 (s, 3H).

Synthesis of CS-FT: CS-FT conjugate was synthesized using EDC and NHS as coupling reagents. For the synthesis, a mixture of DMSO and buffer solution (acetic acid/sodium acetate) with a 1:1 vol ratio was prepared as a solvent. CS (1.0 g) was dissolved in 50 ml of the solvent at 40 °C. FA (0.78 g) and TK (0.48g) was dissolved in 20 ml of the solvent and reacted with EDC (0.92 g) and NHS (0.64 g) at room temperature for 15 min to activate the terminal carboxyl groups. The activated solution was then applied to the CS solution, and a conjugative reaction was conducted at 40 °C for 24 h. After reaction, the solution was dialysed against water for 5 days (molecular weight cutoff, 3500Da). After dialysis, we obtained CS-FT by freeze-drying and kept the product in a refrigerator before use.

Synthesis of CS-FTP: A mixture of DMSO and buffer solution (acetic acid/sodium acetate) with a 1:1 vol ratio was prepared as a solvent. CS-FT (0.5 g) was dissolved in 50 ml of the solvent at 40 °C and reacted with EDC (0.2 g) and NHS (0.1 g) at room temperature for 15 min to activate the terminal carboxyl groups. PAZ (0.005 g) was dissolved in 5 ml of the solvent at 40 °C and was applied to the CS-FT solution, and a conjugative reaction was conducted at 40 °C for 24 h. After reaction, the solution was dialysed against water for 5 days (molecular weight cutoff, 3500Da). After dialysis, we obtained CS-FTP by freeze-drying and kept the product in a refrigerator before use.

Preparation of CS-FTP-gel: CS-FTP-gel were prepared by mixing aqueous CS-FTP polymer and laccase solution. Hydrogels (100 ml) were prepared in 1 ml vials at 37 °C. 75 μL of the CS-FTP polymer solution and 25 ml of laccase solution were simply mixed and gently shaken.

Measurement of viscoelastic properties: We performed rheological analysis of the hydrogels using a rheometric fluid spectrometer with a 25 mm plate geometry. In the rheological experiments, hydrogel samples were prepared on the plate in the instrument. We performed dynamic time sweeps on hydrogel samples in various conditions. We monitored the elastic modulus (G') and viscous modulus (G'') at 10% of strain and a frequency of 0.1 Hz at 37 °C.

Measurement of cellular VEGFR1/2 and hypoxia: 4T1 cells were seeded in 96-well plates at a density of 1×10^4 $well^{-1}$. After incubation overnight at 37 °C, samples were added to each well and incubated for 1 h. For hypoxia measurement, the old medium was replaced with serum-free DMEM containing 2 μM hypoxia reagent (Image-iT, Thermofisher, USA) and incubated for 20 min. For VEGFR1/2 measurement, cells were incubated with polyclonal rabbit anti-flk-1 primary antibody (Invitrogen) for 1 h. Cells were then rinsed and exposed to Alexafluor 568 goat anti-rabbit IgG secondary antibody (Invitrogen). All of the cells were washed, for measurement under a microplate reader (SpectraMax M2, Molecular Device).

DO measurement: For hydrogel, we measured DO levels non-invasively throughout hydrogels using commercially available sensor patches (Presens, Regensburg, Germany). For cell culture, we measured DO levels non-invasively throughout oxygen sensor foil (Presens, Regensburg, Germany). To measure oxygen levels around cells, the polymer solutions were added on top of the sensors, which were immobilized in each well of a 96-well plate, and then mixed with laccase solutions.

Tumor xenograft model: Xenograft tumor model was established by the subcutaneous injection of 4T1 cells (1×10^7 cells) into the selected positions of the athymic BALB/c nude mice. To determine tumor size, the longest length and width of the tumor were measured by a caliper every other day, and the tumor volume was calculated as length $\times$ width^2 $\times$ 0.5. The experiments were repeated for at least five times.

Tumor orthotopic models: The 4T1 cells (5×10^6 cells) were injected in their right side of mammary fat pad to establish an orthotopic breast cancer model. The mice in orthotopic murine model were randomly divided into four groups. To determine tumor size, the longest length and width of the tumor were measured by a caliper every other day, and the tumor volume was calculated as length $\times$ width^2 $\times$ 0.5. The experiments were repeated for at least five times.

Micro-PET/CT imaging: Tumor-bearing mice that received different treatments were intravenously injected with 100 μL of a saline containing ^{18}FMISO (150 μCi per mouse). After 1 h, PET/CT images were captured by an Inveon Animal-PET/CT Scanner (Siemens Preclinical Solutions, Knoxville, TN, USA). The data were processed and reconstructed on the workstation.

Histological analysis: The major organs (heart, liver, spleen, lung, and kidney) and the tumor were dissected and sectioned for H&E staining. To explore the therapeutic effect of the combination therapy, tumors were also stained for VEGFR1, VEGFR3, PDPN, and endothelial cell marker CD31. All the histological analysis were carried out by Servicebio (Wuhan, China).

***Antimetastasis treatment*:** At the end of study, mice were sacrificed. The lungs were collected and photographed. The metastatic tumor modules in the lungs were numerated by using a microscope.

Statistical Analysis: Data were examined statically using the SPSS17.0 statistical analysis software. All the error bars indicated mean $\pm$ s.d. Student t-test or one-way analysis of variance (ANOVA) followed by Tukey's honestly significant difference (HSD) test was applied for comparison between two groups or among multiple groups, respectively.

CRediT authorship contribution statement

Shi-Xiong Chen: conceived and designed the project. performed in vitro experiments. performed in vivo experiments.All authors discussed the results and commented on the manuscript. **Ji Zhang:** conceived and designed the project. performed in vivo experiments. All authors discussed the results and commented on the manuscript. **Fengfeng Xue:** performed in vitro experiments. All authors discussed the results and commented on the manuscript. **Wei Liu:** performed in vivo experiments. All authors discussed the results and commented on the manuscript. **Yichen Kuang:** performed in vitro experiments. All authors discussed the results and commented on the manuscript. **Bingxin Gu:** performed

in vivo experiments. All authors discussed the results and commented on the manuscript. **Shaoli Song:** Supervision, supervised the project. All authors discussed the results and commented on the manuscript. **Hangrong Chen:** Supervision, supervised the project. All authors discussed the results and commented on the manuscript..

Declaration of competing interest

The authors declare no known competing financial interest.

Acknowledgment

This work was supported by the National Key Research and Development Program of China (Grant No. 2021YFB3801001), the National Natural Science Foundation of China (Grant Nos.32030061), and the Key Program for Basic Research of Shanghai (Grant No. 19JC1415600, 21JC1406000). All the animal experiments were performed with the approval of the Fudan University Experimental Animal Center, and the animal biomedical research authorization numbered is 2020-Cancer hospital-JS220.

Appendix A. Supplementary data

Supplementary data to this article can be found online at https://doi.org/10.1016/j.bioactmat.2022.08.002.

References

[1] J.J. Yeh, W.Y. Kim, Targeting tumor hypoxia with hypoxia-activated prodrugs, J. Clin. Oncol. 33 (2015) 1505–1508.
[2] J.A. Bertout, S.A. Patel, M.C. Simon, Hypoxia and metabolism series - TIMELINE the impact of O-2 availability on human cancer, Nat. Rev. Cancer 8 (2008) 967–975.
[3] G. Bergers, L.E. Benjamin, Tumorigenesis and the angiogenic switch, Nat. Rev. Cancer 3 (2003) 401–410.
[4] P. Vaupel, Hypoxia and aggressive tumor phenotype: implications for therapy and prognosis, Oncol. 13 (2008) 21–26.
[5] V. Bhandari, C. Hoey, L.Y. Liu, E. Lalonde, J. Ray, J. Livingstone, R. Lesurf, Y. J. Shiah, T. Vujcic, X.Y. Huang, S.M.G. Espiritu, L.E. Heisler, F. Yousif, V. Huang, T. N. Yamaguchi, C.Q. Yao, V.Y. Sabelnykova, M. Fraser, M.L.K. Chua, T. van der Kwast, S.K. Liu, P.C. Boutros, R.G. Bristow, Molecular landmarks of tumor hypoxia across cancer types, Nat. Genet. 51 (2019) 308.
[6] O. Tredan, C.M. Galmarini, K. Patel, I.F. Tannock, Drug resistance and the solid tumor microenvironment, J. Natl. Cancer Inst. 99 (2007) 1441–1454.
[7] P. Vaupel, A. Mayer, Hypoxia in cancer: significance and impact on clinical outcome, Cancer Metastasis Rev. 26 (2007) 225–239.
[8] Y.-Q. Cheng, Y.-X. Yue, H.-M. Cao, W.-C. Geng, L.-X. Wang, X.-Y. Hu, H.-B. Li, Q. Bian, X.-L. Kong, J.-F. Liu, D.-L. Kong, D.-S. Guo, Y.-B. Wang, Coassembly of hypoxia-sensitive macrocyclic amphiphiles and extracellular vesicles for targeted kidney injury imaging and therapy, J. Nanobiotechnol. 19 (2021) 451.
[9] H. Chen, J. Deng, X. Yao, Y. He, H. Li, Z. Jian, Y. Tang, X. Zhang, J. Zhang, H. Dai, Bone-targeted erythrocyte-cancer hybrid membrane-camouflaged nanoparticles for enhancing photothermal and hypoxia-activated chemotherapy of bone invasion by OSCC, J. Nanobiotechnol. 19 (2021) 342.
[10] J. Qiao, M.Y. Wang, M.H. Cui, Y.X. Fang, H.N. Li, C. Zheng, Z.L. Li, Y.N. Xu, H. M. Hua, D.H. Li, Small-molecule probes for fluorescent detection of cellular hypoxia-related nitroreductase, J. Pharm. Biomed. Anal. 203 (2021), 114199.
[11] H. Zhang, C.C.L. Wong, H. Wei, D.M. Gilkes, P. Korangath, P. Chaturvedi, L. Schito, J. Chen, B. Krishnamachary, P.T. Winnard, V. Raman, L. Zhen, W.A. Mitzner, S. Sukumar, G.L. Semenza, HIF-1-dependent expression of angiopoietin-like 4 and L1CAM mediates vascular metastasis of hypoxic breast cancer cells to the lungs, Oncogene 31 (2012) 1757–1770.
[12] P. Wardman, Electron transfer and oxidative stress as key factors in the design of drugs selectively active in hypoxia, Curr. Med. Chem. 8 (2001) 739–761.
[13] X.Q. Li, Y.C. Pan, C. Chen, Y.F. Gao, X.L. Liu, K.Y. Yang, X.W. Luan, D.T. Zhou, F. Zeng, X. Han, Y.J. Song, Hypoxia-responsive gene editing to reduce tumor thermal tolerance for mild-photothermal therapy, Angew. Chem. Int. Ed. 60 (2021) 21200–21204.
[14] X.J. Shi, S.H.P. Sung, M.M.S. Lee, R.T.K. Kwok, H.H.Y. Sung, H.X. Liu, J.W.Y. Lam, I.D. Williams, B. Liu, B.Z. Tang, A lipophilic AIEgen for lipid droplet imaging and evaluation of the efficacy of HIF-1 targeting drugs, J. Mater. Chem. B 8 (2020) 1516–1523.
[15] R.K. Jackso, L.P. Liew, M.P. Hay, Overcoming radioresistance: small molecule radiosensitisers and hypoxia-activated prodrugs, Clin. Oncol. 31 (2019) 290–302.
[16] R.M. Phillips, Targeting the hypoxic fraction of tumours using hypoxia-activated prodrugs, Cancer Chemother. Pharmacol. 77 (2016) 441–457.
[17] S.K. Sriraman, B. Aryasomayajula, V.P. Torchilin, Barriers to drug delivery in solid tumors, Tissue Barriers 2 (2014), e29528.
[18] Y. Fu, D. Cen, T. Zhang, S. Jiang, Y. Wang, X. Cai, X. Li, G. Han, Implantable fibrous scaffold with hierarchical microstructure for the 'on-site' synergistic cancer therapy, Chem. Eng. J. 402 (2020), 126204.
[19] J.M. Brown, W.R. William, Exploiting tumour hypoxia in cancer treatment, Nat. Rev. Cancer 4 (2004) 437–447.
[20] L.H. Patterson, S.R. McKeown, AQ4N: a new approach to hypoxia-activated cancer chemotherapy, Br. J. Cancer 83 (2000) 1589–1593.
[21] W.P. Steward, M. Middleton, A. Benghiat, P.M. Loadman, C. Hayward, S. Waller, S. Ford, G. Halbert, L.H. Patterson, D. Talbot, The use of pharmacokinetic and pharmacodynamic end points to determine the dose of AQ4N, a novel hypoxic cell cytotoxin, given with fractionated radiotherapy in a phase I study, Ann. Oncol. 18 (2007) 1098–1103.
[22] W.D. Tap, Z. Papai, B.A. Van Tine, S. Attia, K.N. Ganjoo, R.L. Jones, S. Schuetze, D. Reed, S.P. Chawla, R.F. Riedel, A. Krarup-Hansen, M. Toulmonde, I. Ray-Coquard, P. Hohenberger, G. Grignani, L.D. Cranmer, S. Okuno, M. Agulnik, W. Read, C.W. Ryan, T. Alcindor, X.F.G. del Muro, G.T. Budd, H. Tawbi, T. Pearce, S. Kroll, D.K. Reinke, P. Schoffski, Doxorubicin plus evofosfamide versus doxorubicin alone in locally advanced, unresectable or metastatic soft-tissue sarcoma (TH CR-406/SARC021): an international, multicentre, open-label, randomised phase 3 trial, Lancet Oncol. 18 (2017) 1089–1103.
[23] W.R. Wilson, M.P. Hay, Targeting hypoxia in cancer therapy, Nat. Rev. Cancer 11 (2011) 393–410.
[24] Y.Z. Wang, Y. Xie, J. Li, Z.H. Peng, Y. Sheinin, J.P. Zhou, D. Oupicky, Tumor-penetrating nanoparticles for enhanced anticancer activity of combined photodynamic and hypoxia-activated therapy, ACS Nano 11 (2017) 2227–2238.
[25] C.G. Qian, P.J. Feng, J.C. Yu, Y.L. Chen, Q.Y. Hu, W.J. Sun, X.Z. Xiao, X.L. Hu, A. Bellotti, Q.D. Shen, Z. Gu, Anaerobe-inspired anticancer nanovesicles, Angew. Chem. Int. Ed. 56 (2017) 2588–2593.
[26] K. Zhang, Y.D. Zhang, X.D. Meng, H.T. Lu, H. Chang, H.F. Dong, X.J. Zhang, Light-triggered theranostic liposomes for tumor diagnosis and combined photodynamic and hypoxia-activated prodrug therapy, Biomaterials 185 (2018) 301–309.
[27] S.C. Yang, Z.H. Tang, C.Y. Hu, D.W. Zhang, N. Shen, H.Y. Yu, X.S. Chen, Selectively potentiating hypoxia levels by combretastatin A4 nanomedicine: toward highly enhanced hypoxia-activated prodrug tirapazamine therapy for metastatic tumors, Adv. Mater. 31 (2019), 1805955.
[28] S.X. Chen, F.F. Xue, Y.C. Kuang, S.Y. Chen, D.L. Sheng, H.R. Chen, A self-activating nanovesicle with oxygen-depleting capability for efficient hypoxia-responsive chemo-thermo cancer therapy, Biomaterials 269 (2021), 120533.
[29] M. Miranda-Galvis, Y. Teng, Targeting hypoxia-driven metabolic reprogramming to constrain tumor progression and metastasis, Int. J. Mol. Sci. 21 (2020) 5487.
[30] H. Phuengkham, L. Ren, I. Shin, Y.T. Lim, Nanoengineered immune niches for reprogramming the immunosuppressive tumor microenvironment and enhancing cancer immunotherapy, Adv. Mater. 31 (2019), 1803322.
[31] L.M. Kranz, M. Diken, H. Haas, S. Kreiter, C. Loquai, K.C. Reuter, M. Meng, D. Fritz, F. Vascotto, H. Hefesha, C. Grunwitz, M. Vormehr, Y. Husemann, A. Selmi, A. N. Kuhn, J. Buck, E. Derhovanessian, R. Rae, S. Attig, J. Diekmann, R. A. Jabulowsky, S. Heesch, J. Hassel, P. Langguth, S. Grabbe, C. Huber, O. Tureci, U. Sahin, Systemic RNA delivery to dendritic cells exploits antiviral defence for cancer immunotherapy, Nature 534 (2016) 396.
[32] O.A. Ali, N. Huebsch, L. Cao, G. Dranoff, D.J. Mooney, Infection-mimicking materials to program dendritic cells *in situ*, Nat. Mater. 8 (2009) 151–158.
[33] O.A. Ali, D. Emerich, G. Dranoff, D.J. Mooney, *In situ* regulation of DC subsets and T cells mediates tumor regression in mice, Sci. Transl. Med. 1 (2009), 8ra19.
[34] N. Huebsch, D.J. Mooney, Inspiration and application in the evolution of biomaterials, Nature 462 (2009) 426–432.
[35] E.S. Place, N.D. Evans, M.M. Stevens, Complexity in biomaterials for tissue engineering, Nat. Mater. 8 (2009) 457–470.
[36] M.M. Martino, F. Tortelli, M. Mochizuki, S. Traub, D. Ben-David, G.A. Kuhn, R. Muller, E. Livne, S.A. Eming, J.A. Hubbell, Engineering the growth factor microenvironment with fibronectin domains to promote wound and bone tissue healing, Sci. Transl. Med. 3 (2011), 100ra89.
[37] M.C. Cushing, K.S. Anseth, Hydrogel cell cultures, Science 316 (2007) 1133–1134.
[38] A. Thakur, R.I. Scheinman, V.R. Rao, U.B. Kompella, Pazopanib, a multitargeted tyrosine kinase inhibitor, reduces diabetic retinal vascular leukostasis and leakage, Microvasc. Res. 82 (2011) 346–350.
[39] K.M. Park, S. Gerecht, Hypoxia-inducible hydrogels, Nat. Commun. 5 (2014) 4075.
[40] L.Z. Feng, L. Cheng, Z.L. Dong, D.L. Tao, T.E. Barnhart, W.B. Cai, M.W. Chen, Z. Liu, Theranostic liposomes with HypoxiaActivated prodrug to effectively destruct hypoxic tumors post-photodynamic therapy, ACS Nano 11 (2017) 927–937.
[41] S.S. Li, A.Q. Xie, H. Li, X. Zou, Q.X. Zhang, A self-assembled, ROS-responsive Janus-prodrug for targeted therapy of inflammatory bowel disease, J. Contr. Release 316 (2019) 66–78.
[42] S. Miyamoto, S. Kakutani, Y. Sato, A. Hanashi, Y. Kinoshita, A. Ishikawa, Drug review: Pazopanib, Jpn. J. Clin. Oncol. 48 (2018) 503–513.
[43] N.S. Chatterjee, R. Anandan, M. Navitha, K.K. Asha, K.A. Kumar, S. Mathew, C. N. Ravishankar, Development of thiamine and pyridoxine loaded ferulic acid-grafted chitosan microspheres for dietary supplementation, Journal of Food Science and Technology-Mysore 53 (2016) 551–560.
[44] F. Jiao, W.Q. Qin, R.Z. Liu, X.J. Wang, Adsorption mechanism of 2-mercaptobenzothiazole on chalcopyrite and sphalerite surfaces: Ab initio and spectroscopy studies, Trans. Nonferrous Metals Soc. China 25 (2015) 2388–2397.
[45] R.C. Minussi, G.M. Pastore, N. Duran, Potential applications of laccase in the food industry, Trends Food Sci. Technol. 13 (2002) 205–216.

[46] X.B. Liu, G.N. Qu, Q. Yu, N. Zhang, L. Wang, J. Wang, Synthesis of poly(ethylene glycol) grafted polyamidoamine dendrimer hydrogels and their temperature and pH sensitive properties, Polym. Sci. B 62 (2020) 400–410.
[47] H.E. Abaci, R. Truitt, S. Tan, S. Gerecht, Unforeseen decreases in dissolved oxygen levels affect tube formation kinetics in collagen gels, Am. J. Physiol. Cell Physiol. 301 (2011) C431–C440.
[48] A. Billard, L. Pourchet, S. Malaise, P. Alcouffe, A. Montembault, C. Ladaviere, Liposome-loaded chitosan physical hydrogel: toward a promising delayed-release biosystem, Carbohydr. Polym. 115 (2015) 651–657.
[49] R. Tamate, T. Ueki, Y. Kitazawa, M. Kuzunuki, M. Watanabe, A.M. Akimoto, R. Yoshida, Photo-dimerization induced dynamic viscoelastic changes in ABA triblock copolymer-based hydrogels for 3D cell culture, Chem. Mater. 28 (2016) 6401–6408.
[50] Z. Li, D. Zhu, Q. Hui, J. Bi, B. Yu, Z. Huang, S. Hu, Z. Wang, T. Caranasos, J. Rossi, X. Li, K. Cheng, X. Wang, Adv. Funct. Mater. 31 (2021), 2004377.
[51] H. Lan, F. Lin, Q. Zhou, L. Huang, K. Jin, Strategies to improve drug distribution in solid tumor, Int. J. Clin. Exp. Med. 9 (2016) 658–667.
[52] J.C. Li, D. Cui, Y.Y. Jiang, J.G. Huang, P.H. Cheng, K.Y. Pu, Near-infrared photoactivatable semiconducting polymer nanoblockaders for metastasis-inhibited combination cancer therapy, Adv. Mater. 31 (2019), 1905091.
[53] C.J.P. Silva, G. Liebsch, R.J. Meier, M.S. Gutbrod, E.R. Balmayor, M. van Griensven, A new non-invasive technique for measuring 3D-oxygen gradients in wells during mammalian cell culture, Front. Bioeng. Biotechnol. 8 (2020) 595.
[54] J. Zhang, W. Xia, P. Liu, Q. Cheng, T. Tahirou, W. Gu, B. Li, Chitosan modification and pharmaceutical/biomedical applications, Mar. Drugs 8 (2010) 1962–1987.
[55] Z. Abedian, A.A. Moghadamnia, E. Zabihi, R. Pourbagher, H.R. Nouri, H. Tashakorian, M. Ghasemi, N. Jenabian, Anticancer properties of chitosan against osteosarcoma, breast cancer and cervical cancer cell lines, Caspian. J. Intern. Med. 10 (2019) 439–446.
[56] D.L. Xia, P.P. Xu, X.Y. Luo, J.F. Zhu, H.Y. Gu, D. Huo, Y. Hu, Overcoming hypoxia by multistage nanoparticle delivery system to inhibit mitochondrial respiration for photodynamic therapy, Adv. Funct. Mater. 29 (2019), 1807294.
[57] H. Min, J. Wang, Y.Q. Qi, Y.L. Zhang, X.X. Han, Y. Xu, J.C. Xu, Y. Li, L. Chen, K. M. Cheng, G.N. Liu, N. Yang, Y.Y. Li, G.J. Nie, Biomimetic metal-organic framework nanoparticles for cooperative combination of antiangiogenesis and photodynamic therapy for enhanced efficacy, Adv. Mater. 31 (2019), 1808200.
[58] S. Loges, M. Mazzone, P. Hohensinner, P. Carmeliet, Silencing or fueling metastasis with VEGF inhibitors: antiangiogenesis revisited, Cancer Cell 15 (2009), 167-160.
[59] D.R. Bielenberg, B.R. Zetter, The contribution of angiogenesis to the process of metastasis, Cancer J. 21 (2015) 267–273.
[60] S. Urner, L. Planas-Paz, L.S. Hilger, C. Henning, A. Branopolski, M. Kelly-Goss, L. Stanczuk, B. Pitter, E. Montanez, S.M. Peirce, T. Makinen, E. Lammert, Identification of ILK as a critical regulator of VEGFR3 signalling and lymphatic vascular growth, EMBO J. 38 (2019), e99322.